Bi-monthly • May - June • 2020 • Issue No. 371 ISSN: 0976-2108

BARC NEWSLETTER

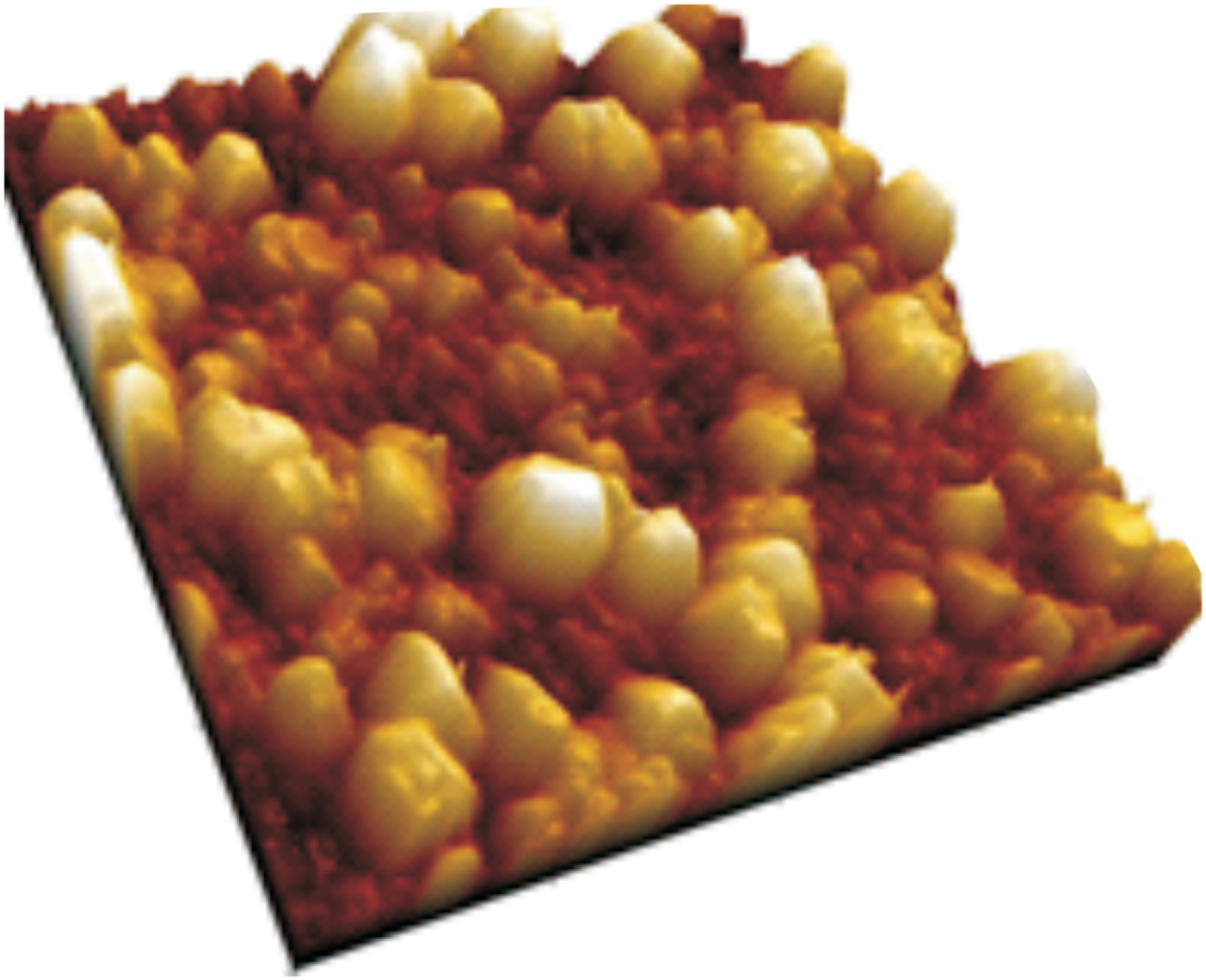

AFM Surface Topography of Single Zincated Aluminium Surface

This page is intentionally left blank

CONTENTS

This page is intentionally left blank

Development of Nanocrystalline UO_2 Coating on 1S Al Substrate

A Neutron Sensor Material for Fabrication of High Sensitivity Fission Counters

Subir Kumar Ghosh*, Jalaj Varshney and Vivekanand Kain
Materials Processing and Corrosion Engineering Division
Raghvendra Tiwari
Materials Science Division
Vijay Karki
Fuel Chemistry Division

Abstract

Fission counters (FCs) are gas filled detectors in which charged fission fragments are formed due to the impact of incident neutrons on fissile Uranium and the resulting charges are collected as signal current on the application of high voltage across the electrodes. The generation of charged particles in FCs depends purely on the interaction of fissile material with neutron. The preferred fissile material used is Uranium-235 (^{235}U), but Uranium-238 (^{238}U) and Thorium-232 (^{232}Th) can also be used for the required applications. The fissile materials are normally introduced within FCs in the form of coating/thin films on suitable substrates, such as SS, Inconel, Al (for low activation) etc. One of the primary considerations to choose a material for the base substrates is the minimization of unwanted secondary radiation interactions in the reactor environment which increase the background, reduce detector efficiency and limits its dynamic range. In addition, presence of impurity elements, such as Co (in SS and Inconel), generates very high energy gamma radiation followed by neutron capture which increases difficulties in handling such detectors. In view of these problems, development of high sensitivity FCs with 1S Al as base material and with UO_2 coating with desired thickness and uniformity has been initiated. However, due to the presence of tenacious Al_2O_3 layer on Al substrate, direct deposition of coatings on it develops issues like cracking and peeling off. In order to address these issues, in the present study, a suitable chemical/electrochemical modified alloy zincating process was adopted to deposit a Zn coating on Al by galvanic displacement and subsequently electrolytically deposit Cu underlayer to engineer the Al surface for UO_2 deposition. Subsequently, the UO_2 coating was applied by DC electrodeposition. The whole tetralayer UO_2/Cu/Zn/Al composite coating structures and their growth behaviour were investigated in detail using atomic force microscope (AFM), field emission scanning electron microscope (FESEM), Rutherford Backscattering Spectroscopy (RBS) and secondary ion mass spectrometry (SIMS). Finally, the entire coatings process has been successfully implemented for the deposition of adherent uniform UO_2 coating on large scale Al tubes as a technology demonstration for the development of high sensitivity FCs in DAE, India.

Keywords: UO_2 Coating, Fission Counter, Zincating, Surface Engineering, Electrodeposition, FESEM, SIMS, RBS.

Introduction

Fission counter/chambers are essential components of Nuclear Instrumentation Systems (NIS) to monitor power, power regulation as well as for reactor protection. FCs are used to monitor 10 decades of flux in source (0.1 nv-10^5 nv) , intermediate (10^3 nv to 10^9 nv) and power ranges (10^7 nv to 10^9 nv) [1-3] where 'nv' represents numbers of neutrons per square centimeter per second. In terms of reactor power, they can be used to monitor reactor power from 8-10% of the FP (Full Power) to 150% FP [2-3]. Fission counters use fissile materials to generate signal through neutron induced nuclear fission reaction. Fission fragments thus generated ionize the filled gas and get discharged at the respective electrodes producing current signal. Depending upon neutron energy spectrum of the reactor, fissile materials, such U-235, U-238 and Th-232 [4-6], are normally used in FCs. In contrast to limited energy operation regime and high gamma sensitivity B-based counter [2], Uranium based counter has wide operation range along with very good gamma discrimination ability. A thorough understanding of performance related factors in FCs was done previously based on the demanding operating environment

and the requirement of gamma tolerance [5,7-8]. Also, the processing electronics plays an important role in providing optimized performance of the measurement system. The efficiency of FCs primarily depends on the noise generated from background radiation, secondary nuclear reactions and by processing electronics. Various technological improvements have significantly reduced the noise associated with processing electronics leading to in higher S/N ratio. In these FCs, fissile materials coated base electrode acts as signal electrode and other electrode acts as ground. These signal electrodes are made up of metal/alloys with requisite properties such as:

- Very good radiation as well as high temperature resistance in terms of mechanical and dimensional stability.
- Very low neutron absorption cross-section.
- Should not produce secondary radiation upon exposure to reactor environment or upon nuclear reaction that interfere with the signal radiation for better signal to noise ratio (S/N).
- The coated fissile material should remain adherent to the electrode surface throughout the life time of the detector.

So far, uranium based FCs that have been developed in India are UO_2 coated on SS-321 or on Inconel-600 or on Ti substrates. Typical sensitivity achieved from these detectors is in the range of 0.1 to 0.6 cps/nv. The basic problem in considering SS-321 or Inconel-600 is due to the presence of trace amount of Co which comes as impurity along with Ni alloy content and undergoes neutron capture reaction in reactor environment thereby produces Co-60 isotope. This Co-60 isotope is a well-known high energy gamma source and interferes strongly with signal generated due to fission products inside FCs. In addition, it hampers handling of the detectors post neutron flux measurement exercise. In fact, FCs are frequently used while start-up operation as well as power regulation of research reactors and start up of PHWRs. And once the reactor is in its full scale operation mode in case of PHWRs, these detectors are withdrawn and stored in a safe place which requires manual handling and transportation. The need of the hour is to produce such FCs which apart from addressing the aforementioned issues must be having higher sensitivity with counting efficiency of the order of ~1 cps/nv or higher while retaining overall detector dimensional portability.

In order to overcome all these complications, a suitable electrode material was necessary which can withstand high radiation environment without dimensional deformation, produce no or minimum secondary radiation upon irradiation with minimum interference with the actual neutron induced signals. Considering all these parameters, high purity Al (i.e. AISI 1050 or 1S grade) was selected as supporting signal electrode due to its inherent low neutron absorption cross section (0.16 b). It may be noted that FCs made of Al electrodes have been used for neutron flux measurement by French since long time. However, the major challenge in using Al electrode is difficulty in coating of the fissile UO_2 on its surface due to the presence tenacious thin Al_2O_3 layer which prevents good adhesion with overlayer coatings. Apart from this, the sensitivity of FCs also depends on UO_2 coating thickness and its uniformity across the working length of the detector, design of the detector and energy of the neutrons. For the first time in the country, an indigenous attempt was made to apply adherent and uniform UO_2 thin coating on Al surface to fabricate very high sensitivity neutron detector for use in research reactors like Dhruva and PHWRs start-up operation.

In this report, development of adherent and uniform thickness natural UO_2 coating on 1S Al surface by suitable chemical/electrochemical surface engineering approach has been presented. The fundamentals of systematic oxide removal from Al surface followed by application of Zn interlayer using a simple galvanic displacement reaction and Zn-root growth into Al matrix along with overgrowth on Al surface providing better mechanical anchoring effect for excellent adhesion were discussed. AFM and FESEM were used to understand surface topography evolution while zincating. The zinc layer thickness and deposition rate was further ascertained by RBS technique because of dual nature (simultaneous dissolution/deposition) of zincating process. Electrolytic deposition of UO_2 layer on post zincated Al surface and its detail characterization by focused ion beam (FIB) cut cross-section of UO_2/Cu/Zn/Al interface using FESEM investigation. All these microstructural features along with elemental distribution across UO_2/Cu/Zn/Al tetralayer interfaces were further substantiated by detail SIMS depth profiling analysis. The whole sequential coatings processes

were scaled up to production level and showed indigenous capability to deposit uniform adherent UO_2 coating on Al tubes for large scale production of FCs.

Surface Engineering of Al Surface

Pure Al and its alloys find tremendous industrial applications due to their low density (2.7 $g.cm^{-3}$), good mechanical strength (UTS: 310 MPa), formability, very high abundance (~8% of earth crust) and corrosion resistance. Because of low hardness and poor wear resistance for any functional application, suitable surface modifications of Al and its alloys are required. However, presence of highly protective Al_2O_3 layer on Al surface hinders any surface structure alterations. In fact, application of suitable coatings of other metals and alloys on Al surface without removal of Al_2O_3 layer was seen to provide poor adhesion leading to cracking or peeling off from the surface leading to a redundant exercise.

Over the years through extensive investigations, a very simple but critical chemical surface modification process known as "*zincating*" which is a 'Galvanic displacement" reaction was adopted to apply first a very thin Zn layer on Al with simultaneous in-situ removal of alumina layer for depositing Zn coating followed by subsequent coatings or thin films providing strong adhesion with base Al substrate. The overall chemical reaction of zincating process associated with hydrogen evolution can be written as

$$3Zn(OH)_4^{2-} + 2Al + 2H_2O = 2AlO_2^{2-} + 3Zn + 3H_2 + 10OH^- \quad (1)$$

In this investigation, a simple modified alloy zincating technique applied twice known as double zincating (DZ) treatment was adopted to obtain adherent uniform thin layer of Zn film on 1S grade Al surface [9]. The Al substrate was first polished with SiC papers followed by diamond paste until 0.02 µm average roughness was achieved. The polished Al substrates were first cleaned in alkali solution containing 30 $g.l^{-1}$ NaOH for 30 s at 65 °C. The zincating electrolyte was consisted of ZnO, NaOH, tri-sodium citrate, NaCN and $FeCl_3$. Prior to first zincating, the substrates were desmutted in 50 vol% nitric acid solution for 30 s at room temperature. The first or single zincating (SZ) was carried out on desmutted Al surface by immersing in the zincating solution for a duration of 60 s at room temperature. After SZ, Zn-coated substrates were again subjected to 50 vol% HNO_3 dissolution for 45 s followed by second dip in zincating solution (double zincating) for a duration of 60 s for re-growth of Zn film.

Post zincating i.e. the Zn film coated Al substrates were subjected to copper coating from a copper strike bath at room temperature for 5 minutes to obtain copper coating. These copper coated Al substrates were then dipped into natural uranium containing uranyl nitrate-oxalate solution as described earlier [10-12] to deposit nat-UO_2 thin coating by DC electrodeposition. Post deposition, the UO_2 coated samples were heat treated in normal air atmosphere at 120 °C for 1 h in order to remove adsorbed moister and to ensure coating adhesion to substrate at higher temperature and to understand structural changes within the layered composite film structure.

Characterization of Zincated Al and UO_2 Coated Surface

Surface morphology of polished Al and Zn-coated Al specimen were investigated under AFM (NX-10, Parks Systems) to study the roughness, nucleation, growth and coverage of zinc film on Al substrate. The images were taken in a non-contact mode using Si cantilever. AFM topographic images were recorded over scan areas from 1 micrometer (µm) x 1 micrometer (µm) to 50 µm x 50 µm. Average roughness (R_a) of the zincated surface is the arithmetic mean of the absolute values of the height of the surface profile $h(x)$ and is described as

$$R_a = \frac{1}{L}\int_0^L |h(x)|dx \quad (2)$$

where $h(x)$ is a function that describes the surface profile analyzed in terms of height (h) and position (x) of the sample over the evaluation length L. Since R_a is strongly dependent on scan length L, for comparison, the average roughness (R_a) was calculated from the scan area of 10 µm x 10 µm. The surface morphology of various time-dependent zincated films and nitric acid dipped substrates were further investigated under FESEM with 20 kV of beam energy. Elemental distribution of Zn, Fe and Cu in a zincated film was determined by energy dispersive spectroscopy (EDS) attached with FESEM. The cross-section specimen was prepared by cutting the sample using focused ion beam (FIB) attached with FESEM. The deposited Zn film crystal structure, phase analysis and grain size were studied using Rigaku Smartlab grazing incidence XRD (GIXRD) unit attached with 9 kW rotating anode X-ray generator.

RBS is a non-destructive technique in which the thin film thickness is measured by counting the number of backscattered particles. Here, the thickness and growth rates of Zn films

were estimated by RBS technique. For this, a 4 MeV proton beam was used in Folded Tandem Ion Accelerator (FOTIA) at Bhabha Atomic Research Centre (BARC), India. The detector, a surface barrier detector, was mounted in a backscattering angle θ of 160° from the incident beam. The thickness of Zn layer was estimated from the number of counts detected by two separate detectors kept at 160° to incident proton beam. Finally, these counts were averaged out for calculation of the Zn layer thickness. The total yield (Y) can be expressed as

$$Y = N_p N_t \frac{d\sigma}{d\Omega} \Omega \quad (3)$$

and the number of target nuclei per unit area (N_t) is given by

$$N_t = (N_A\, t) / A \quad (4)$$

where N_p is the number of projectiles per second, $\frac{d\sigma}{d\Omega}$; the backscattering cross section, $d\Omega$; the solid angle, N_A; the Avogadro's number t; the thickness in mg.cm^{-2} and A is atomic weight of target element Zn and Al. Here, the alloy addition of Fe was considered as negligible because of absence of any measurable signal. The obtained experimental counts were normalized dividing the total yield by total numbers of projectiles.

Depth distribution analyses of all the elements present in the layered as-deposited and heat-treated samples were carried out using a magnetic sector based Cameca IMS-7f secondary ion mass spectrometer (SIMS) equipped with both oxygen and Cs^+ primary ion beams. A Cs^+ primary ion beam with an impact energy of 5 keV and beam current of 105±5 nA was utilized for the depth distribution analysis of elements (O, Al, Fe, Cu, Zn and U) in the tetralayer composite coating. To minimize the matrix effects due to the presence of different layer composition, MCs^+-SIMS ('M' being the element of interest) mode was selected. In order to remove the crater edge effects, primary beam was raster scanned over an analysis region of 150 µm × 150 µm and secondary ions were collected from an analysis area of ~8.3 µm in diameter at the centre of raster area using a field aperture of 100 µm. The pressure in the analysis chamber was maintained at ~8.3×10^{-9}mbar during the analysis to minimize the mass interferences due to the presence of residual gases. For meaningful conclusions of the SIMS depth profile data, the conversion of sputtered time to depth profile data is crucial. Hence, the depth of the craters formed during SIMS analysis was measured by using 3D optical profilometer and the depth measured was utilized to calibrate the sputtering time axis to depth (µm).

Since the UO_2 coating is porous in nature [10-11], in order to check thickness uniformity across the surface, an inconel disc (33 mm dia.) was coated with UO_2 and alpha count from specific area of 6 mm diameter at different spots was measured for a constant duration using alpha spectrometer.

Results and Discussions

Surface Topography of Zincated Surface

Progressive galvanic displacement of Al layer by Zn during zincating was carried out on polished Al substrate with an average roughness, R_a of 10.8±2 nm. Gradual Zn nucleation, growth and surface coverage on Al surface were investigated ex-situ in detail under AFM. Fig.1 (a)-(d) shows progressive change in 3-D surface morphologies of polished Al surface to zincated surface with respective process steps. It is pertinent to see that post single zincating, the average surface roughness of 10.8±2.0 nm of polished Al surface increased to 154±2.2 nm at 60 s associated with

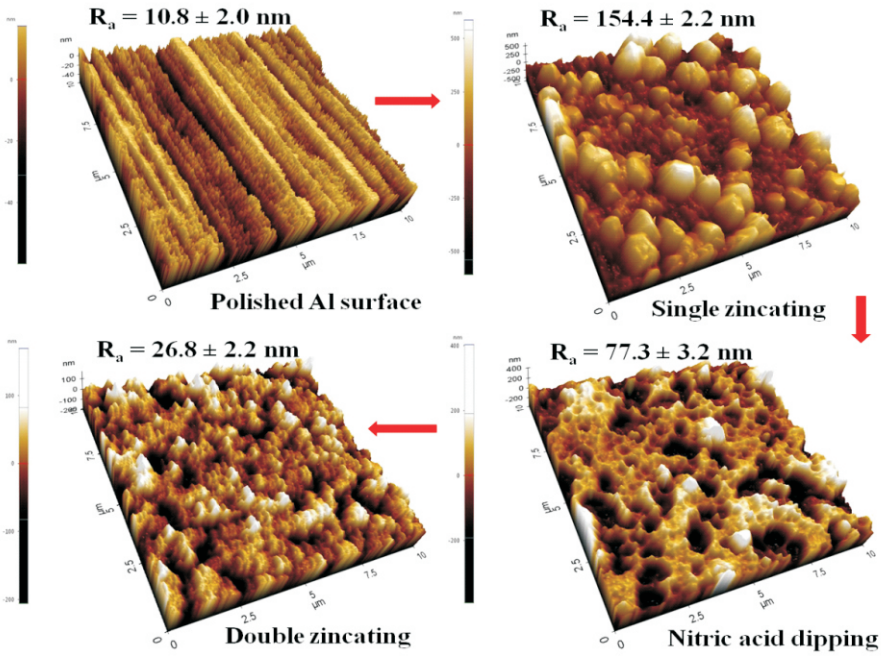

Fig.1: Progressive evolution of 3-D AFM surface topography of (a) polished Al surface to (b) SZ Al surface (60 s) to (c) nitric dip SZ Al surface to (d) DZ Al surface (60 s).

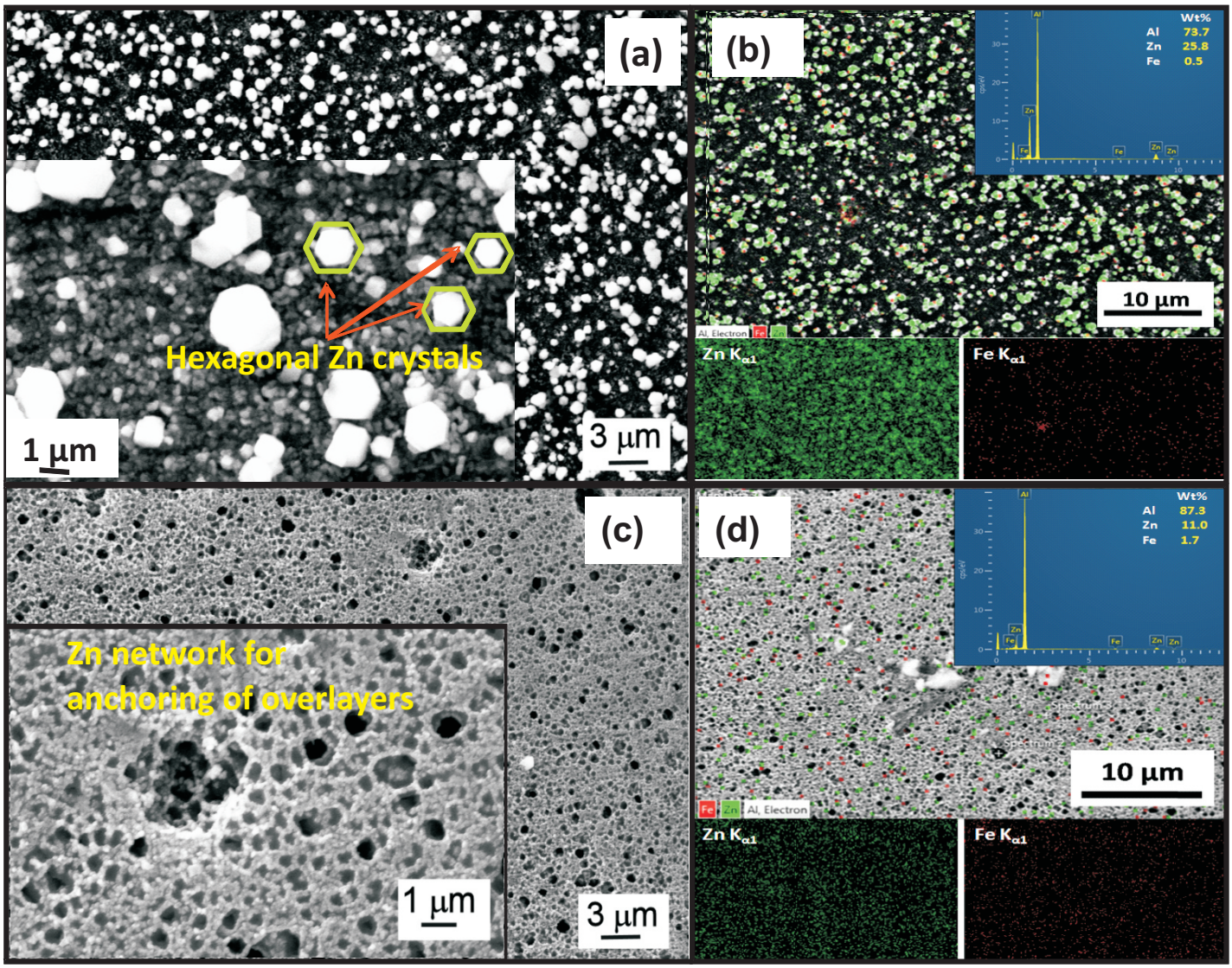

Fig.2: FESEM surface topography of (a) single zincated Al surface after 1 min.; inset showing bimodal distribution of Zn particles along with large hexagonal particles; (b) EDS elemental mapping of single zincated surface; (c) double zincated surface after 1 min; inset showing net like fine grained porous Zn deposition but with full coverage of Zn including inside deep pit; (d) EDS elemental mapping of double zincated surface showing uniformity across the surface.

growth of non-uniform large and small Zn grains. This is attributed to faster rate of galvanic displacement reaction and scattered nucleation phenomena. Prior to DZ immersion, the single zincated Al surface was dipped in 50% nitric acid for 45 s to strip out the first Zn-layer. The nitric acid dip Al surface is shown in Fig. 1(c) which basically consists of numerous small pits with wide range in sizes (nm to µm) with faceted walls. Such pits are actually imprint of previous Zn-grain down-growth into the Al matrix and the bigger hexagonal shape faceted holes are indication of growth of Zn crystallites. The R_a value of nitric etched microporous surface is 77.3±3.2 nm which is relatively smoother in comparison to single zincated Al surface. After second zincating dip of nitric acid etched Al surface results into smooth and uniform distribution of Zn grains with uniform coverage can be seen in Fig. 1(d). The R_a value of DZ surface comes down to 96.4±3.4 nm at 60 s dip.

In order to visualize better in X-Y plane with greater depth of view in larger scale, zincated Al surfaces were further investigated under FESEM. Fig. 2 (a) shows single zincated Al surface covered with large hexagonal shaped faceted Zn crystals along with smaller Zn crystals having bimodal distribution [9] corroborating AFM observations. An enlarged view can be seen in the inset image of Fig. 2(a) where growth of large distinct hexagonal Zn crystals is visible. Fig. 2(b) shows EDS elemental mapping of single zincated surface confirming presence of Zn, Fe from zinc film and Al from substrate. It is noted that very small quantity of Fe is present as alloy content within the Zn layer that deposited during zincating as shown in EDS spectrum (inset of Fig. 2(b)). The FESEM image of DZ

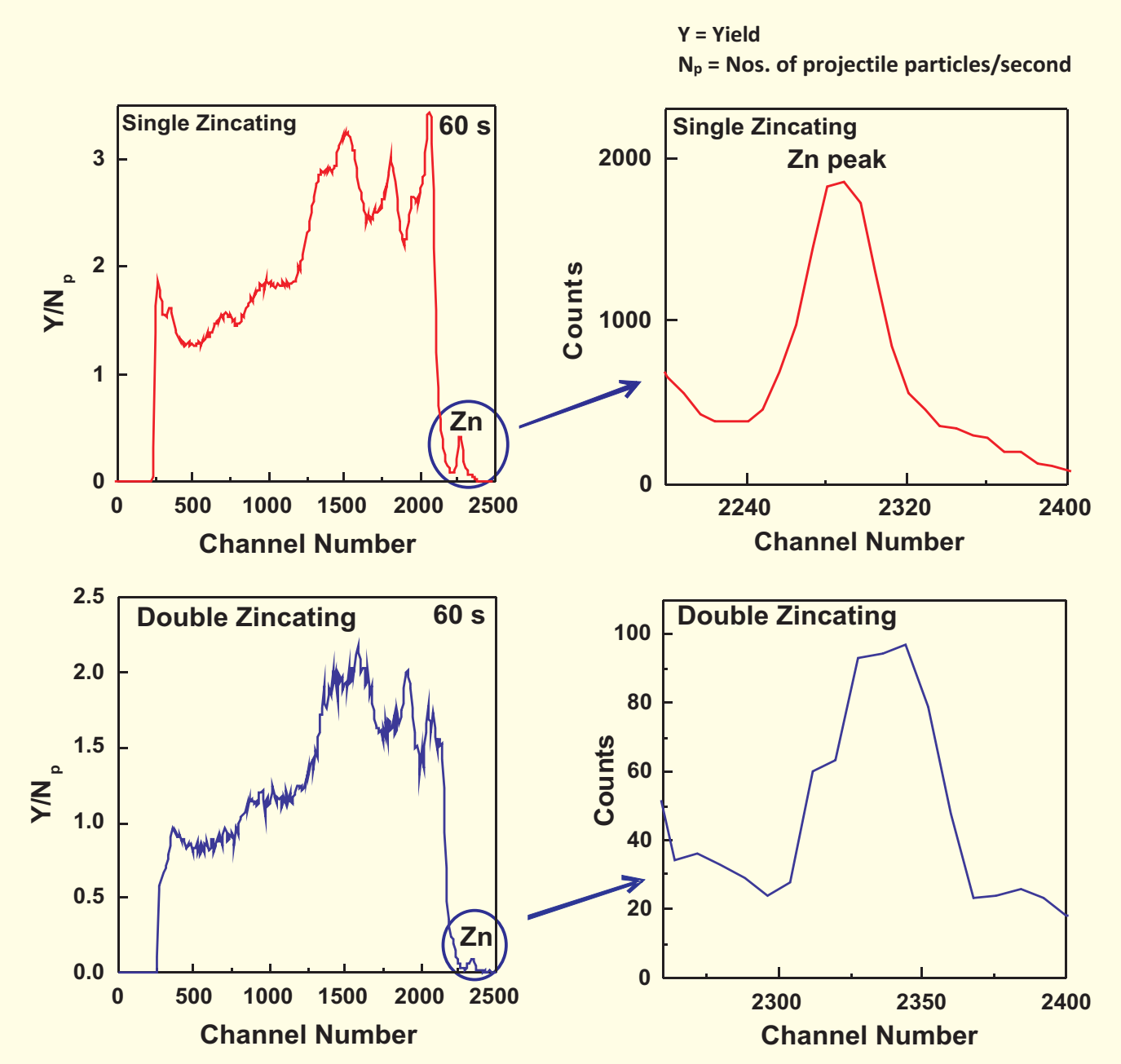

Fig.3: Normalized backscattered counts vs. channel number plot obtained from single and double zincated Al substrate using RBS measurement. Right hand side plots are corresponding enlarged view of Zn peak.

Al surface (Fig. 2(c)), in contrast, shows fairly uniform covered Zn layer with smooth surface topography consisting of fine grained networked Zn film. An enlarged view of the DZ surface clearly shows uniform Zn coverage even inside the dip pits (inset of Fig. 2(c)). In fact, this kind of net-like Zn film structure provides anchoring effect of the overlayer grown on it leading to better adhesion of Cu overlayer and subsequently UO_2 film. The corresponding elemental distribution across the surface shows Zn and Fe are uniformly distributed on Al (Fig. 2(d)). Hereto, the presence of very small quantity of Fe alloy content into the Zn layer was confirmed from EDS point spectrum (inset of Fig. 2(d)).

Zn Film Estimation by RBS

Post zincating quantitative estimation of Zn layer thickness on Al substrate is a crucial task in controlling the respective overlayers thickness and adhesion so that the adhesion of applied UO_2 films remains unaffected and to minimize the secondary signal generation in the assembled detector. Displacement of Al atom by Zn^{2+} ion via galvanic process is a kinetically vigorous phenomenon and results into very rough Al/Zn interface which makes it difficult to determine quantitatively the Zn layer thickness via microscopic techniques. Apart from this, zincating being an atomistic exchange phenomenon between Al

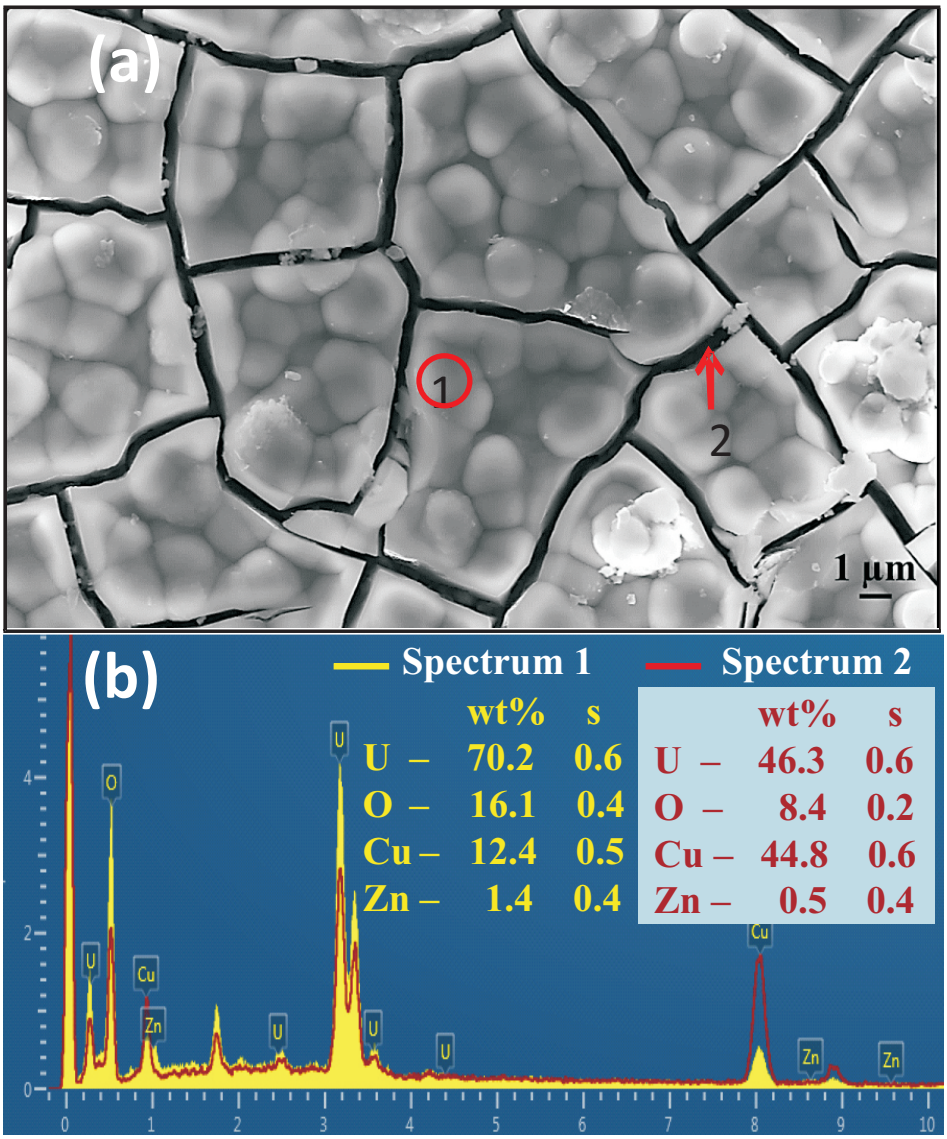

Fig.4: FESEM surface topography of UO_2 film deposited for 45 min and corresponding elemental composition at different points on the surface determined by EDS.

and Zn, simple gravimetric determination of Zn layer thickness led to erroneous conclusion. Since, while zincating, the dissolution of Al occurs via galvanic displacement as well as via alkali etching which makes the process simultaneous competition between Zn deposition and Al dissolution. On the other hand, nuclear technique like RBS being a non-destructive technique, was employed here to determine the Zn deposition quantitatively in terms of mass deposited and average thickness. Progressive increase in zincating duration was found to increase in Zn layer thickness (image not shown here) [9]. The normalized backscattered counts spectra of SZ and DZ Al surface for identical zincating duration of 60 s are shown in Fig. 3. The small peak corresponding to higher channel number represents signal due to Zn atom and the board spectrum at lower channel numbers originates from Al substrate and background noise. The zoomed image of Zn peaks are shown at right side of the Fig.3 were considered for calculation of Zn atom mass per unit area. Using equation 3, the typical Zn-layer thickness calculated was 37.60 $mg.dm^{-2}$ and 13.47 $mg.dm^{-2}$ at 60 s for SZ and DZ respectively. The Zn layer growth rate calculated was 0.47 $mg.dm^{-2}.s^{-1}$ for SZ (= 6.58 $nm.cm^{-2}.s^{-1}$ assuming compact Zn growth with theoretical density 7.2 $g.cm^{-3}$) and 0.17 $mg.dm^{-2}.s^{-1}$ (= 2.38 $nm.cm^{-2}.s^{-1}$) for DZ. It is clear that the Zn-growth rate in SZ is nearly three times faster than DZ. Such a large variation in growth rate is attributed to poisoning of post SZ nitric etch Al surface by the retained Zn, and Fe atoms as confirmed by EDS analysis [9]. Presence of such electrochemically noble elements has basically reduced the effective galvanic driving force which is nothing but difference in open circuit potential of galvanic couple. These scattered foreign elements not only reduced the Zn deposition rate but also helped in forming fine grain deposit by blocking AlO^{2-} ions path thereby results into smooth uniform deposition of Zn across the Al surface during DZ.

Surface Morphology of Electrodeposited UO_2 Film on Zincated Al

Post zincating, the Zn covered Al substrates were given a Cu undercoat to protect the Zn layer from corrosion during UO_2 deposition from alkaline complexed uranyl solution. The Cu undercoat was given from a commercial Cu-strike bath for a duration of 5 minutes by applying DC current of 5 $A.dm^{-2}$. After Cu-strike coating, the Al substrate was dipped into uranyl oxalate complex bath for UO_2 deposition as described elsewhere [10-12]. In order to study the time-dependent growth of UO_2 film and $Al/Zn/Cu/UO_2$ interface study, the UO_2 deposition was conducted at three different time durations of 15 min, 30 min and 45 min. Fig.4 (a) shows the top surface morphology of as-deposited UO_2 thin film which shows granular growth along with numerous cracks. Fig. 4(b)

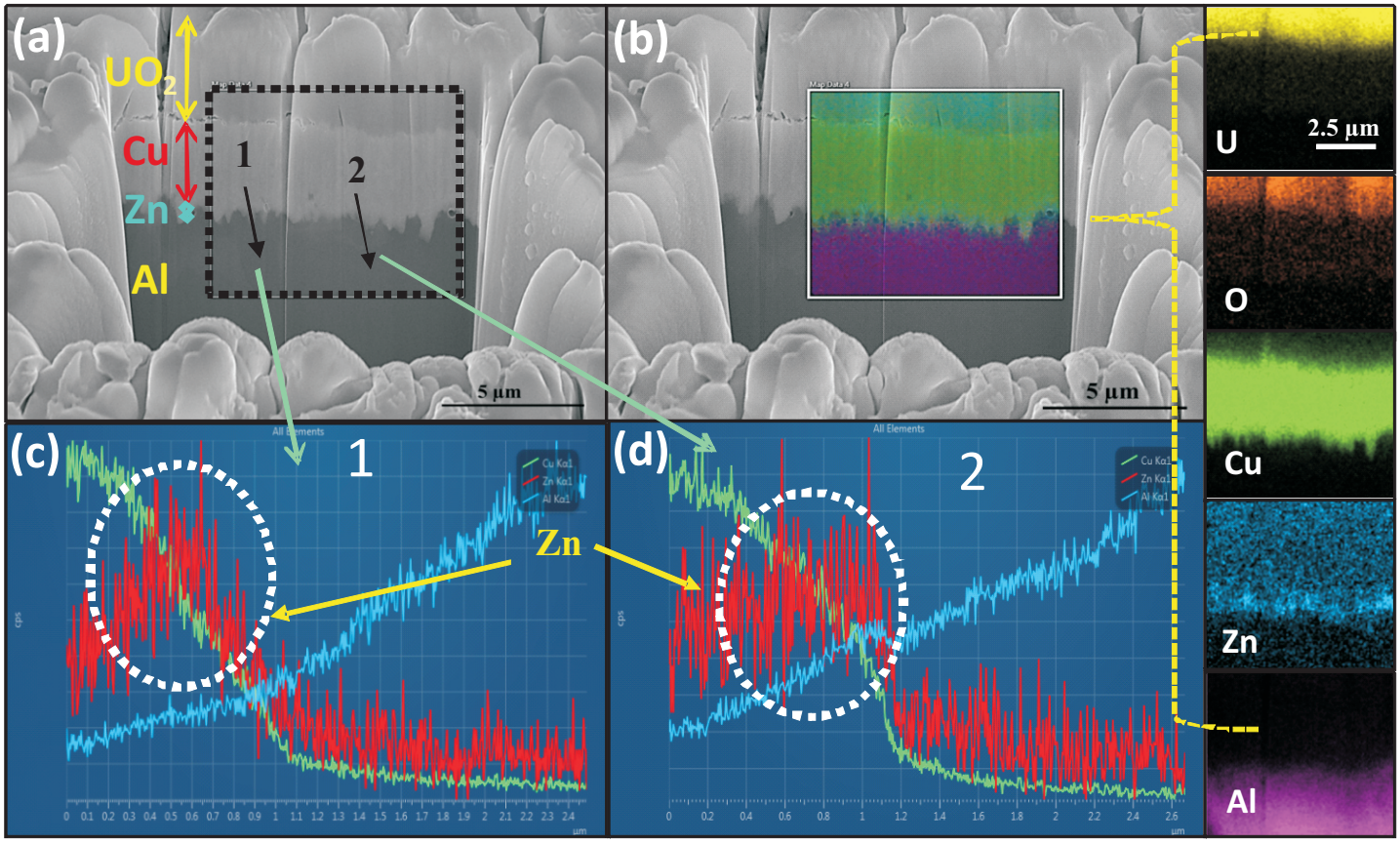

Fig.5: FIB cut cross-section FESEM image of as-deposited UO_2 coating (45 min) showing (a) tetralayer UO_2/Cu/Zn/Al coating on Al surface, individual layer thickness and microstructure of the coatings, (b) EDS elemental mapping of U, O, Cu, Zn and Al across the selected coating/substrate interface showing individual element distribution in respective layers and very rough Zn/Al interface imparting chemical/mechanical anchoring, (c&d) EDS line scan from Cu layer to Al showing direct evidence of presence of very thin layer of Zn on Al.

shows the EDS point spectra corresponding to film top region (Region 1) & crack regions (Region 2) separately in order to confirm the presence of UO_2 layer deep inside the cracks. There is a clear variation in the composition of uranium between film top and cracks regions. The lower wt% of U inside the crack represents lower thickness of UO_2 film and more wt% of Cu from underneath layer. It also confirms that these cracks are in UO_2 films sub-surface region without exposing the underneath copper surface. In fact, the presence of such cracks makes this film porous and the deposited UO_2 film is nanocrystalline in nature as confirmed by GIXRD as well as HRTEM investigations in previous investigations [10-12].

For detailed structural information of the coating and integrity of individual layers attachments on respective substrates, cross-sectional investigation was done on FIB-cut UO_2/Cu/Zn/Al tetralayer composite coating. Fig. 5(a) shows typical trilayer contrast image structure since the fourth layer Zn being very thin and adjacent to Cu, the Z-contract is practically abolished.

Typical ~3-4 µm UO_2 layer could be seen as top layer on underneath ~3 µm Cu layer which is firmly attached to the Al substrate.

To reveal the existence of very thin Zn layer and its significant role on subsequent overlayer growth, and confirming individual layers chemical composition and their distribution, EDS elemental area mapping on selected cross-sectional region (Fig. 5(b)) was done which provided clear evidences of thin but scattered Zn layer on Al due to its vigorous kinetic nature of deposition. Typical thickness of Zn layer was ~ 300-400 nm as estimated from colored elemental Zn map. In fact, the Zn/Al interface is rather rough which in fact provides both chemical as well mechanical anchoring effects for good adhesion. This EDS area mapping also shows the sequence of individual layers from Al to UO_2 in the tetralayer coating structure. The existence of Zn layer was further ascertained by EDS line scan chemical analysis at two different interfacial regions as shown in Figs. 5(c&d). A clear Zn peak confirms its existence. It may be noted that the line spectrum of Fe as alloying element in Zn is omitted here for better

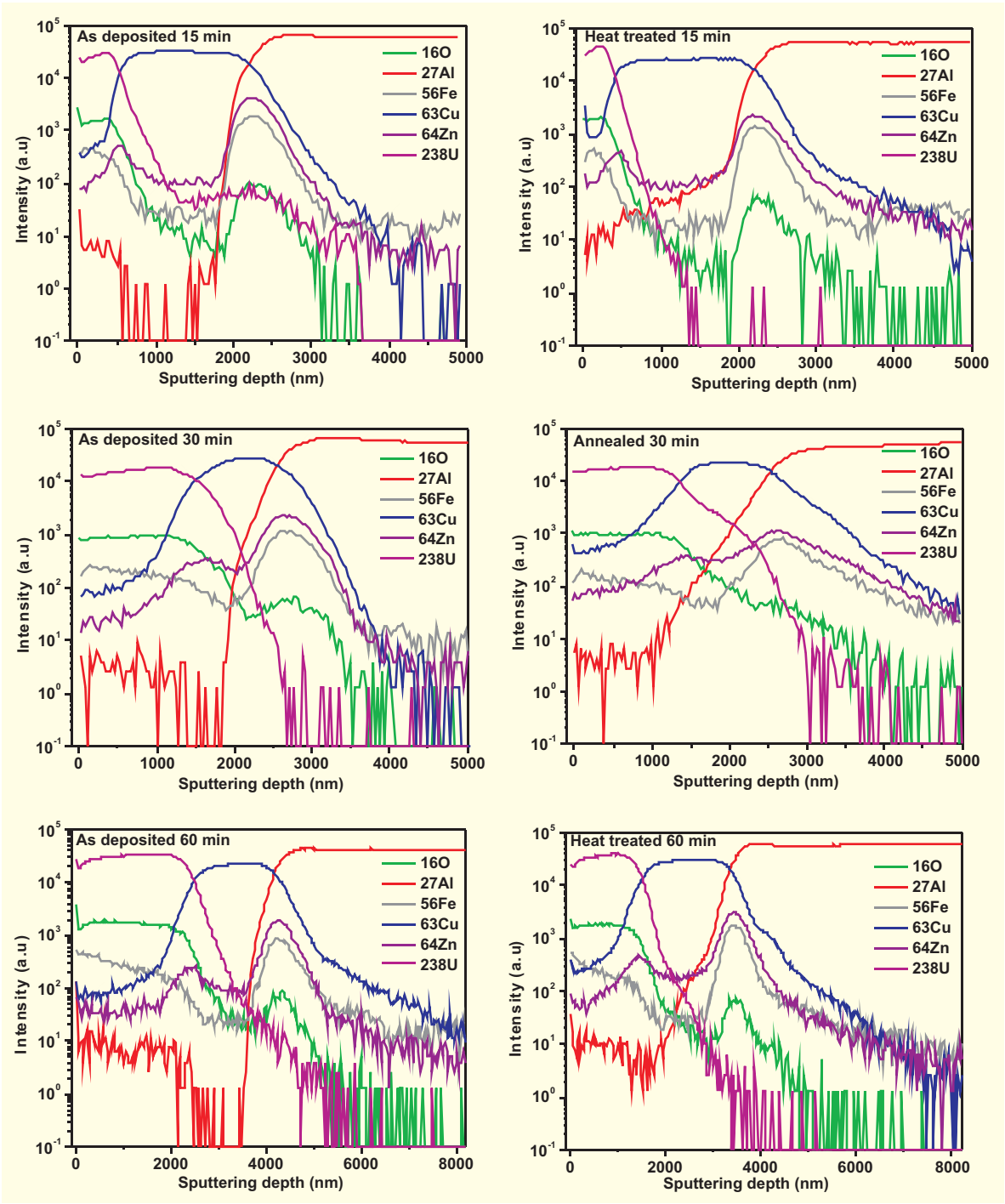

Fig.6: SIMS depth profile plots of UO_2 coated Al sample along with Cu and Zn interlayers for samples with 15 min, 30 min and 45 min UO_2 deposition duration and corresponding heat-treated samples (120 ^{o}C).

representation. It is also mentioned here that the UO_2/Cu interface is rather weak due to the presence of scattered voids confirming the top surface FESEM morphology. In fact, this is well known that oxide/metal bonding is rather weak in comparison to metal/metal bonding as evidences from Cu/Zn and Zn/Al interfaces. But the partial bonding between UO_2 and Cu could be attributed to UO_2/Cu_2O or UO_2/CuO spinel formation at the UO_2/Cu interface. The detail mechanism of good adhesion between UO_2/Cu is a matter of future investigation.

SIMS investigation of Layered Structure

SIMS depth profile analyses of various elements O, Al, Fe, Cu, Zn and U in the as deposited and heat treated samples (120 ^{o}C, 1 h in air) are shown in Fig. 6(a)-(f). The SIMS depth profile of as-deposited samples with UO_2 layer deposition time of 15, 30 and 45 minutes are shown in Fig. 6 (a), (c) and (e) whereas the corresponding annealed samples are shown in Fig. 6 (b), (d) and (f) respectively. It can be visualized for the depth profiles that the uranium and oxygen profiles are coinciding each other which confirms

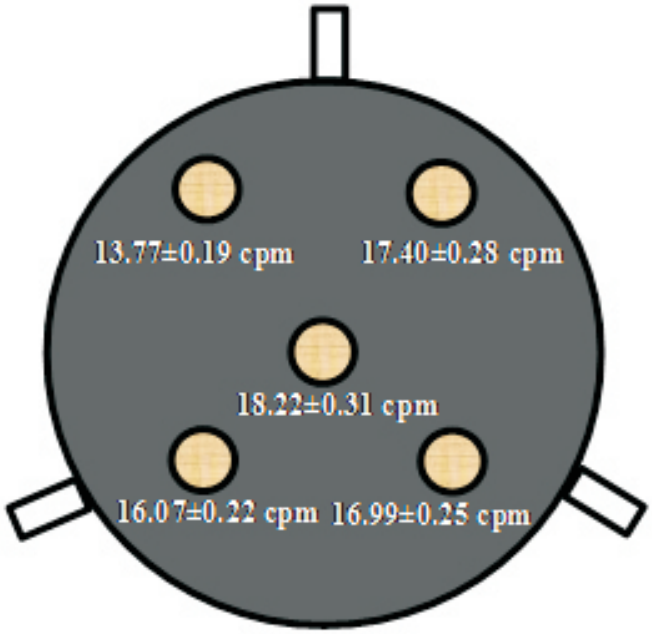

Fig.7: Elemental U mapping data on 6 mm diameter spots using alpha spectrometry showing thin film uniformity across the coated disc (dia. 33 mm).

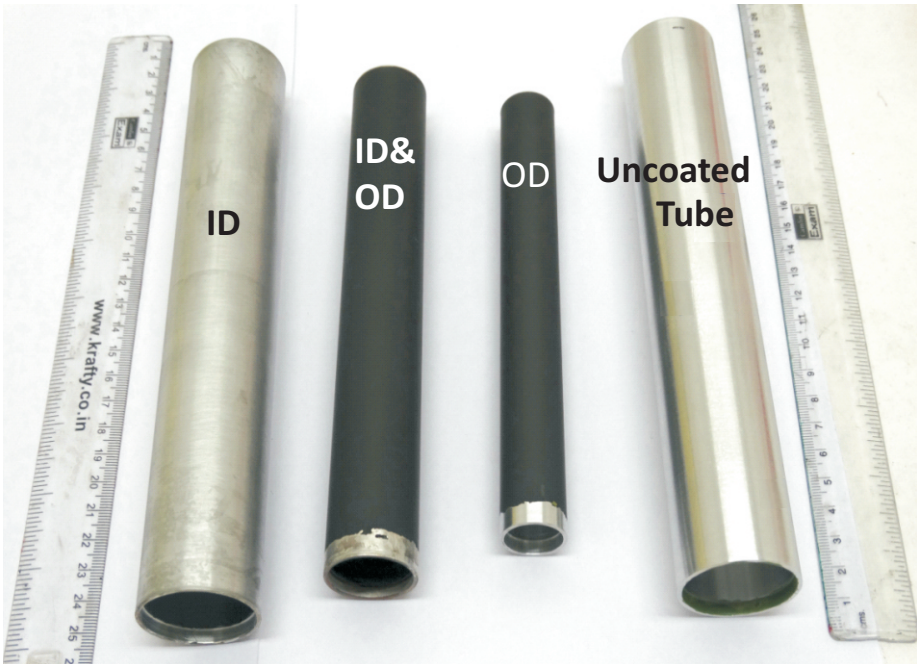

Fig.8: Demonstration of large scale adherent UO_2 coating on ID, ID&OD and OD of 1S Al tubes by adopting chemical/electrochemical surface engineering followed by electrodeposition for fabrication of Fission Counters.

the presence of UO_2 layer at the top surface followed by elements from the top to down sequence as Cu to Zn-Fe and finally the matrix Al confirming the cross-sectional FESEM observations. It is noted that the Fe depth profile follows Zn profile confirming alloy addition of former into the latter. The samples show a well establish interface region of Cu, Zn-Fe layers with Al matrix which concluded the adherence of the Cu-Zn-Fe layer with the Al matrix corroborating the FESEM results. It can be noted from the figures that with increase in the deposition time the thickness of the UO_2 layer increases. The thickness of the UO_2 layer determined from the SIMS depth profile measurements in as-deposited samples are ~461 nm, ~1476 nm and ~2322 nm for 15, 30 and 45 minutes of deposition time respectively. A slight difference in thickness estimation with respect to cross-section FESEM observation is due to porous nature of the film and also due to sampling area (~8.3 μm^2) on the surface consisting of several cracks. Due to lesser density of the UO_2 layer, the sputtering rate by secondary ions was much higher and the depth of the crater formed by sputtering was measured ex-situ under a 3D-optical profilometer. This might have introduced some error while depth calculation. Otherwise, the sequence of elemental layers from top of the surface to Al substrates matches perfectly with the cross-section FESEM results. Post heat-treatment, the thickness of the UO_2 layer in the samples are ~303 nm, ~1357 nm and ~1371 nm for 15, 30 and 45 minutes of deposition respectively. This kind of contraction in UO_2 layer thickness was also observed in our earlier investigation which is attributed to partial crystallization and layer compaction. This concludes that heat treatment basically increases the density of the UO_2 layer. It is also noted from the depth profiles that the Cu layer is inter-diffused in the UO_2 layer after annealing and therefore increases the adhesion.

For determination of deposited UO_2 layer thickness uniformity across the large area surface, a 33 mm diameter inconel disc was coated with UO_2 after suitable surface engineering by applying Ni and Cu interlayers. Post deposition, the as-deposited film was tested at different regions using alpha spectrometry for monitoring emanated alpha rays from nat-U sample consisting of 0.7 wt% U-235 isotope. Fig.7 shows

diagrammatically typical sampling spots of 6 mm diameter from different locations of the disc were chosen for alpha ray counting. The average count rate obtained from different locations are mentioned in the image (Fig.7) and the average value obtained was 16.49±1.73 cpm with relative standard deviation (RSD) of 10% which indicates pretty good thickness homogeneity across the surface in terms of fissile element having several cracks and porosity within the UO_2 films.

For fabrication of high sensitivity FCs, 1S Al was thus considered as an ideal material for depositing fissile materials i.e. UO_2 and following chemical/electrochemical surface engineering technique, an adherent nanocrystalline UO_2 coating with uniform and desired thickness across the surface has been successfully deposited and demonstrated with high reproducibility on large scale. Fig. 8 shows typical uncoated, UO_2 coated Al tubes on outer diameter (OD), inner diameter (ID) and both ID and OD. This coating process has been demonstrated in large quantities.

Conclusion

In this study, modified alloy zincating was adopted for successful removal of alumina layer from the Al surface and simultaneous deposition of thin Zn layer making it enable for depositing subsequent overlayers. Using microscopic techniques, like AFM and FESEM, the microscopic mechanism of Zn deposition and controlling its gain size, uniformity across the Al surface during very fast kinetic galvanic displacement process were monitored. For example, the deposited Zn surface morphology in SZ was highly granular and scattered with bimodal distribution of Zn particles whereas the DZ process gave rise to fine grained Zn along with uniform coverage across the surface. EDS composition analysis of top layer zincated surface confirmed presence of Zn along small quantity of Fe which was deposited as along with Zn as alloying content. The thickness of deposited Zn layer was accurately determined by RBS technique and it was found that the SZ deposition rate was much faster than DZ. The surface morphology of UO_2 coating on Cu/Zn/Al substrate was granular with network of cracks. But EDS elemental composition analysis confirmed the presence of layer of UO_2 even underneath the cracks without exposing the Cu surface. Cross-sectional investigation of FIB cut UO_2/Cu/Zn/Al tetralayer composite structure showed clear sequence of individual layers thickness along with their interface pattern. Both Zn/Al and Cu/Zn interfaces were highly compact and strong with metallic bonds unlike UO_2/Cu interface where scattered nanometer size voids were noticed. It also confirmed the roughness of Al/Zn interface was quiet high due to its vigorous kinetic nature of deposition. The tetralayer coating structure and their sequence was further ascertained by SIMS investigation. Heat-treatment of the deposited coatings led to compaction of the top UO_2 layer with a shrinking in thickness and a slight inert-diffusion among inter layers and top UO_2 was also noticed which basically improved the adhesion of the top UO_2 layer. Finally, for the first-time in DAE, the whole chemical/electrochemical surface engineering process was implemented successfully for deposition of adherent uniform coating of UO_2 on large scale tubular geometry on both ID and OD surfaces for fabrication of FCs.

***Corresponding author**

Dr. Subir Kumar Ghosh

References

1) K. Roy, Nuclear instrumentation for reactor start-up and power regulation, IAEA-RCA regional training course on experimental research reactor physics; Mumbai (India); 15-26 Mar 2004; pp.187-207.

2) H. Boeck, TRIGA reactor main systems, IAEA Report, AIAU—27308, 2007, pp. 1-37.

3) V. K. Mohindra, M. A. Vartolomei, A. McDonald, Fission chambers for CANDU® SDS neutronic trip applications, 28th Annual Canadian Nuclear Society (CNS) Conference, 2007 June 03-06, Saint John, New Brunswick, Canada.

4) G. D. Hickman, A Miniature Fast Fission Counters, Nuclear Instruments and Methods, 13(1961) 190-196.

5) M. Giot, L. Vermeeren, A. Lyoussi, C. Reynard-Carette, C. Lhuillier, P. Mégret, F. Deconinck, B. S. Gonçalves, Nuclear instrumentation and measurement: a review based on the ANIMMA conferences, EPJ Nuclear Sci. Technol. 3 (33) (2017) 1-49.

6) V. R. Parikh, High energy neutron detection by thorium coated fission counters, Proceedings of 11th International Conference on Cosmic Rays, Budapest, (1969) 375-379.

7) G. P. Srivastava, Electronics in nuclear power programme of India-An overview, Sadhana, 38 (2013) 897-924.

8) V. Balagi, K. R. Prasad, S. K. Kataria, Effect of High Gamma

Background on Neutron Sensitivity of Fission Detectors, Ind. J. Pure & Appl. Phys. 42 (2004) 390-397.

9) V. Pachchigar, J. Varshney, S. K. Ghosh, V. Kain, Reinvestigation of Nucleation and Growth of Zn on Al surface during Modified Alloy Zincating, Surface and Coatings Technology, 382, (2020) 125191-125201.

10) S. K. Ghosh, J. Varshney, R. Tewari, V. Kain, K. Madangopal, Indigenous Development of Adherent Nanocrystalline UO_2 Thin Films: Heart of Large Scale Fission Counters, BARC Newsletter, July-Aug (2017) 9-16.

11) J. Varshney, S. Rajak, S. K. Ghosh, B. Vishwanadh, R. Tewari, P. U. Sastry, G. K. Dey, Electrosynthesis and Characterization of Nanocrystalline UO_2 from Aqueous Alkaline Electrolyte, RSC Advances, 6, (2016) 112646–112655.

12) S. Rajak, S. K. Ghosh, J. Varshney, A. Srivastava, R. Tewari, V. Kain, Electrochemical investigation of uranyl species reduction in alkaline oxalate electrolyte and microstructural characterization of deposited nanocrystalline UO_2 thin films, Journal of Electroanalytical Chemistry, 812, (2018) 45-53.

In-house developed Scintillators and Pulse Shape Discriminator Algorithm

Detection of Ultra-low Level Alpha Activity in Mixed Radioactive Sources

Mohit Tyagi*, A. K. Singh,
Technical Physics Division
D. G. Parulekar
Technology Development Division
Vidya Thorat, R. K. Mishra, Amar Kumar
Waste Management Division

Abstract

Different types of radiations like alpha, beta, gamma, neutron, etc. can be discriminated by using single crystal scintillators if the decay time consists of more than one component and the relative amplitude depends on the mode of excitation. However, the discrimination of very low alpha activity in presence of high beta activity is difficult due to cross-talk leading to false counting. Ce doped $Gd_3Ga_3Al_2O_{12}$ (GGAG) single crystals have very fast decay time to handle high count rate and able to discriminate different type of radiations with a decent figure of merit. To increase the sensitivity of discrimination and avoid false counting, four different algorithms were developed. With the help of in-house developed detector and algorithms, ultra-low level alpha activity ~0.1 pico-curie from solid samples was successfully detected in presence of ~1 micro-curie beta activity in 10 hrs. with alpha background of 0.1% of Minimum Detectable Limit (MDL).

Keywords: Crystal growth, Scintillator, Radiation Detector, Nuclear Pulse Recognition, Mixed Sample Radiometry.

Introduction

Single crystal scintillators are the most efficient medium for detecting various nuclear radiations [1,2]. Therefore they have numerous applications in nuclear industry, medical, security, academic etc [3]. An ideal scintillator should have the characteristics like high density and effective atomic number, high light yield, fast decay time, high radiation and mechanical hardness, transparent to its own emission etc. No single material can fulfill all the properties and therefore the most suitable scintillator is selected based on the application [4]. Some of the conventionally used halide single scintillators have limitation of detecting charged particles as they have to be encapsulated hermetically due to their hygroscopic nature. The shorter penetrating length of the charged particles makes it difficult to interact with the sealed scintillators.

In addition to the detection, the discrimination of different type of radiations is also necessary in mixed field applications. The discrimination of various radiations like alpha, beta, gamma and neutron can be based on the detection of corresponding pulse height or pulse shape [5]. The pulse height discrimination is useful when different radiation are giving well separated energies like thermal neutron detection by lithium iodide LiI(Eu) scintillators, in presence of low energy gamma backgrounds. However, it is not possible to discriminate pulse heights of low energies in the continuum spectrum from beta or gamma radiations.

Therefore, pulse shape discrimination (PSD) is very useful and essential method to discriminate various types of radiations [6]. PSD can be achieved in the scintillators having more than one decay components whose relative amplitude varies with the type of radiations. There are various techniques to process these different pulses for discriminating the radiations including zero cross over, rise time discrimination, constant time discrimination, wavelet transformation, charge comparison etc [7]. The advance and fast digitizers are replacing the analog techniques as the recorded pulse can be digitized and the required information can be obtained with various states of art algorithms. PSD measurements by using digitizers are usually based on the charges integrated in different time windows. The data filtering is very important for an appropriate selection of the required pulses. However, in case of very feeble presence of one type radiation in another strong radiation, like trace level of alpha contamination in strong beta sources, a single

technique may not be able to detect or may give false counting due to cross-talk, dead time etc.

Therefore, in this communication, we describe the development of fast single crystal scintillators and PSD with multiple filtering to rule out any cross-talk for achieving the detection of ultra-low contamination of alpha in strong beta sources.

EXPERIMENTAL

Detector development

Single crystal of Ce doped $Gd_3Ga_3Al_2O_{12}$ were grown using Czochralski technique in Crystal Technology Section, TPD, BARC. The details of the growth have been reported in our earlier communications [8]. 0.2 atomic % Boron was also co-doped in the starting material to improve the scintillation properties. A thin disk of about 1 mm thickness was cut and optically polished from the grown crystal. The disk was mounted on a photomultiplier tube having ~ 1 inch dia active area of photocathode. The optical grease was used to mount the crystal for better light collection. An aluminized myler was used to cover the top surface of the crystal such that the charged particles may penetrate without much loss and the generated light could be reflected back to the PMT also. Different samples having various mixed concentrations of alpha and beta emitters were kept on top of the detector, in direct contact with the myler. The detector was connected to a desktop 250 MS/s digitizer for the data collection. The HV for PMT was also provided from the desktop digitizer.

Data acquisition

CAEN digitizer DT5790 comes with data acquisition and DPP_PSD firmware using short gate charge to long gate charge ratio method. It is used for samples with beta to alpha ratio up to 10^4. Commercial CAEN software allows storing raw waveform for customized post processing but it only allows ASCII format of file. ASCII data would have been order of Tera Bytes for offline analysis of samples with beta to alpha ratio of 10^7. Hence Linux based data acquisition code was written using CAEN programming manuals to bring down the data storage and measurement time to order of hrs. We could add more pulse shape discrimination algorithms for better rejection of false triggers seen in commercial CAEN PSD firmware for samples with beta to alpha ratio > 10^4. A user specific code was written in C<*gcc*>. GNU scientific library, GSL<*-lgsl*>, was extensively used in developing PSD routines. BARC standard PC was used in dual boot mode. The user can enter the name of <*outfile*> with number of pulses to be acquired as argument to Linux executable. Upon execution, the code starts ramping up HV to detector from 0 to recommended value and then starts writing the binary <*outfile*> till total number of pulses are acquired. Following that the HV is ramped down and acquisition mode is turned off and user is informed on command prompt that N number of pulses are saved in <*outfile*>. For having three runs of each measurement, an internal shell script is used to invoke executable with delay and collect sets of data in files with different suffixes. During development stage High Performance Computing Center (HPCC) at NRG was used for processing large amount of offline raw pulse data.

Data processing

Each sample is stored as 16 bit integer value and hence a 400 sample raw pulse makes 800 bytes in CAEN DT5790. The code for processing is written into four parts. The first part is for reading the binary data in pieces from file in offline mode and from a shared memory buffer object in online mode, second part is for extracting the list of features from pulse data, third part is for comparing the features with preset conditions arrived in development stage for decision on alpha pulse and the fourth one is to store the diagnostics and alpha pulses binary data into <*outfile*> for further display to user as per requirement. It was observed that only single algorithm to discriminate the pulses results in cross talk due to heavy beta background in sample and improper filtering. Hence four filtering methods were used to achieve zero crosstalk and thereby reducing the false detections to 0 for a standard beta source. The standard beta source was counted for order of hrs. & ~1 million beta gamma pulses were processed through sets of PSD with zero pulses detected as alpha. However 4-5 alpha pulses were detected for 10hrs. background counting without any source. This decided the alpha MDL possible for mixed samples which was 10^7 ratio of beta to alpha. These four methods are based on (1) fitting a pre calibrated Mean vs. STD line (2) fitting a Mean vs. Variance curve, (3) a window function method and (4) comparing energy in frequencies [9, 10].

During development phase of detector, for processing large amount of offline raw pulse data, services of High Performance Computing Centre (HPCC) at Nuclear Recycle Group was used.

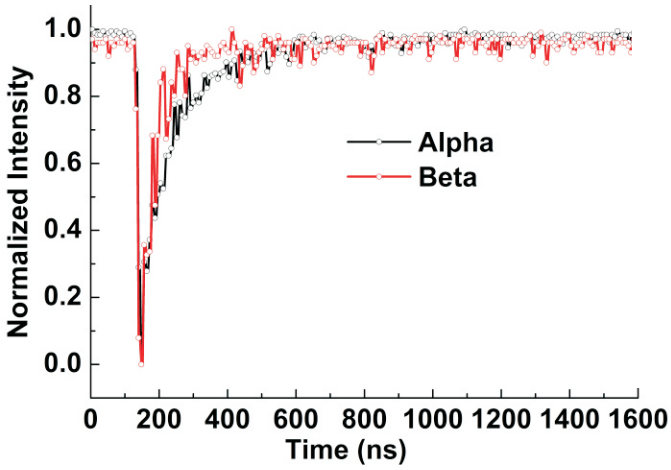

Fig.1a: The raw decay pulses measured for alpha and beta sources and used for the data processing

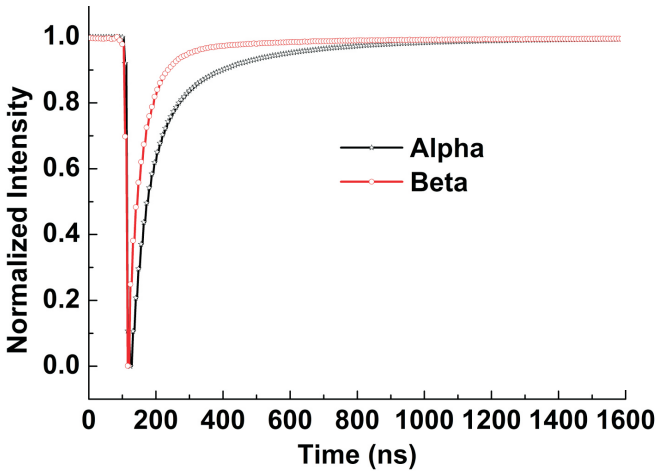

Fig.1b: The average of decay pulses measured for alpha and beta sources

Results and Discussions

Figure 1a shows the single pulse recorded for the alpha and beta sources respectively. The average of about 1000 pulses is shown in figure 1b. The pulses triggered at different time were rejected for the averaging. The decay time consists of mainly two decay components which is a necessary condition for the pulse shape discrimination.

The relative amplitude of these two components depends on the mode of excitation. However, unlike halide crystals, alpha irradiation makes the decay time slower in these crystals. Consequently, the charge integrated in different time window will depend on the mode of excitation. Therefore different algorithms can be used to extract the information from these pulses for a better figure of merit to discriminate low activity of alpha in mixed samples. The pulse shape discrimination based on the charge collection in short and long gates is represented in figure 2. The ratio of alpha and beta activity was 1000:1 in this sample. The X-axis can be calibrated for the energy to discriminate the type of radiations on energy and time scale. The PSD ratio plotted on Y-axis is defined as $(1-Q_l/Q_s)$; where Q_l and Q_s are the charge collected in the user defined long and short gates respectively. These values for these gates were optimized to be 100 and 1000 ns in case of GGAG crystals for the better figure of merit. The faster decay time of these crystals has the advantage of handling the higher count rates. However for the lower activity of alpha in higher beta activity samples, the cross-talk lead to false counting. Therefore multiple algorithms were used.

One of the efficient methods for discrimination is to plot mean vs. standard deviation (std.), or mean vs. variance (var.), of the mixed pulses [10]. The pulses which have not been recorded properly can be also rejected by this method as the mean vs. std. relation will be different than the relation for correctly recorded pulses. Figure 3 shows the plot of std vs. mean of collected pulses. Fitting lines are generated using curve fitting tools.

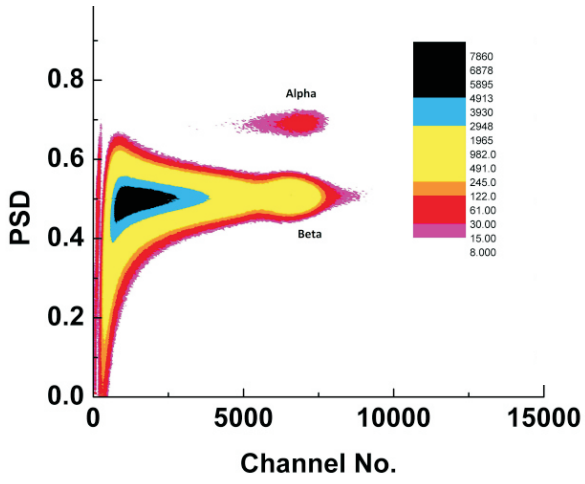

Fig.2: The pulse shape discrimination (PSD) measured with the mixed sample of alpha and beta

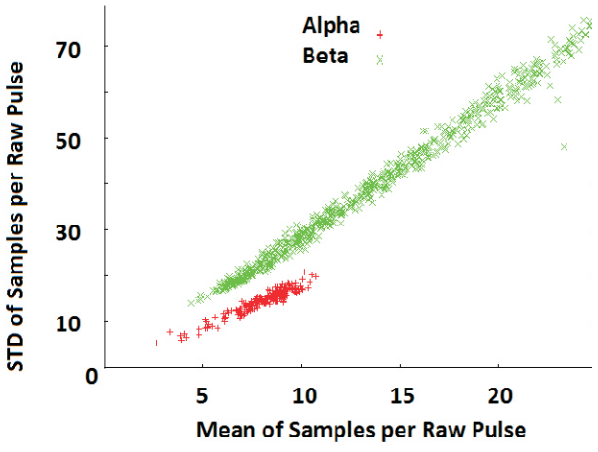

Fig.3: The mean vs. standard deviation (STD.) plot for the mixed source

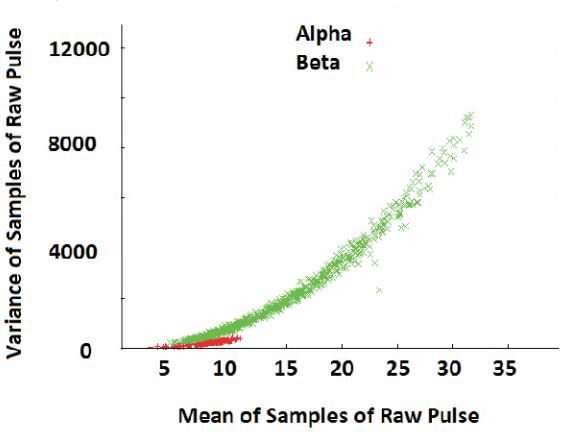

Fig.4: The mean vs. variance plot for the mixed source

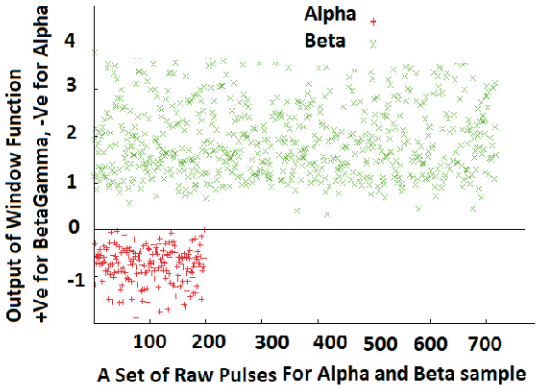

Fig.5: The Window Function plot for the mixed source showing negative polarity for alpha pulses

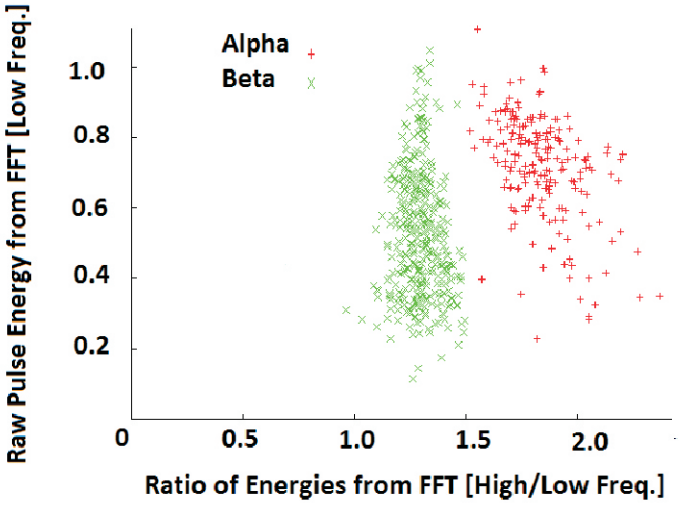

Fig.6: The PSD plot for the mixed source based on the Wavelet Transform method

These fits are used for selection or rejection of alpha pulses. Mean SD and Variance are computed with statistical formulas over N samples. It is seen that when the pulses have short decay time the variance and std is higher for given mean value. It means that samples 'vary' more from mean sample value because pulse decays faster back to baseline. Noise filtering and normalization of pulses is not required for this method and therefore individual pulses can be processed in the real time. Similarly the mean vs. variance can be plotted based on the number of samples in the pulses for a particular type of radiation. Figure 4 represents the plot of mean vs. variance (var.) calculated for the mixed sample. Fits can be generated for selection of alpha pulses.

For further discrimination in an additional method, a window function is designed based on the relative amplitude of the time function for different type of radiations. This window function has different polarity (positive or negative) for different type of radiations (beta or alpha). Figure 5 shows the plot of this window function. In an additional algorithm based on the Wavelet Transform, a time-frequency space is used to decompose the signal over dilated and translated wavelets [10]. A scale function is defined as the energy of the wavelet transform of the signal at a specific scale. Ratio of energy in two scales vs. energy in one scale is shown in Fig.6. Different signals having different decaying components hence the energy components are different in low and high frequency bands. Figure 6 represents this discrimination of alpha and beta radiations using energy patterns in different frequencies. Scale 128 and Scale 512 were selected after fine tuning. Padding of signal was done because scales selected are required to be 2^N for digital implementation in future.

Constraints

The calibration parameters of all PSD algorithms are subject to changes in detector setup. Before measurements, all calibration was required to be done again on standard samples of alpha and beta. It was confirmed before measurements that there is zero crosstalk for measurement time with standard beta source, alpha background below MDL required and practical counting time& efficiency. This prior work was done on offline data. Offline analysis involved solving a computation problem of collecting, transferring and processing large volume of data of order of 100s of Giga Bytes. After successful calibration, a BARC standard PC can be used with calibrated parameters in online mode in which total raw waveform data is not stored.

When sample base activity was above 1 microCurie, pulse pile up effect was witnessed. Overlapping of two short duration beta pulses at peak region made single long decaying 'false alpha pulse' which successfully escaped all four PSD algorithms. These false alpha detections resulted in an increase in MDL compared to when sample had 1 micro Curie base activity. The advantage was because of higher base activity, shorter counting time was possible. With present set up, ~100 hrs are required to count ~10^{10} pulses for samples having base activity of 1microCurie. As the ratio of beta to alpha go above 10^7, alpha background counts in 100 hrs. of counting time must be less than 1 to achieve lower alpha MDL. It was observed that background reduction for longer counting time was not possible due to absence of proper vacuum or air tight enclosure for counting set up. It is essential to achieve alpha background < 1 for required counting time in alpha radiometry for mixed samples having ratio of beta to alpha > 10^7.

Conclusion

The setup was tested in Waste Immobilisation Plant (WIP) active lab to acquire and process mixed radiation pulses from newly developed scintillation detector at rate of 1 Million/Min using standard BARC PC in online mode. Alpha was detected in mixed samples with ratio of beta to alpha being 10^7 with overnight counting. Three runs were carried for each known and unknown set of mixed radioactivity samples. The base activity of sample was ~1microC and 10^9 pulses were acquired within two shift operations. Alpha detection efficiency without Pulse Shape Discriminator (PSD) was ~50%, however due to conservative alpha pulse selection in PSD; pulses were not accepted as alpha until they passed all the four stages of alpha selection logic. Alpha efficiency using PSD therefore was seen around ~10-15% for standard alpha source. The trade-off was efficiency vs. cross talk. When less PSD stages were used then more alpha efficiency was witnessed for alpha standard source &beta pulses were also detected as alpha having poor crosstalk. Hence conservative selection of efficiency figure was done to achieve zero cross talk during counting time for standard beta source. This resulted in validation by correct estimation of alpha ratio in various known and unknown mixed radioactivity samples prepared with Sr and Am activity.

***Corresponding author**

Dr. Mohit Tyagi

Future Work

The detector and Photo Multiplier Tube (PMT) set-up is proposed to be installed for further experimental validation in WIP active lab using commercial air-tight enclosure having sample holder at bottom. Further establishment of pulse recognition radiometry using novel scintillation detector is planned for applications demanding stringent quality control e.g. radio pharmaceutical products.

Acknowledgments

In development stage, expert guidance was given by Ms. Vibhuti, Computer Division for processing large amount of data in practical time frame. ShriA.P.Das, DRHR & Shri Devendra, TDD shared two numbers of terabyte portable disks for collection and transfer of offline pulse data. Authors extend gratitude for constant encouragement and valuable guidance by Head TPD, Head TDD & A.D. NRG.

References

1. C. Dujardin, et al., IEEE Trans. Nucl. Sci. 65 (2018) 1977.
2. M. Nikl and A. Yoshikawa, Advance Optical Materials 3 (2015) 463.
3. P. Lecoq, Nucl. Instrum. Methods Phys. Res. Sect. A 809 (2016) 130.
4. Knoll, G. F. Radiation Detection and Measurement, 2000, John Wiley & Sons, Inc. Fourth edition, Chapter 10 and references therein.
5. A. Syntfeld, et al., IEEE Trans. Nucl. Sci. 52 (2005) 3151.
6. R. A. Winyard, J. E. Lutkin and G. H. McBeth, Nucl. Instrum. Methods 95 (1971) 141.
7. W. H. Miller, M. Diaz de Leon, J. Rad. Anal. & Nucl. Chem.,264 (2005) 163.
8. M. Tyagi, A.K. Singh, S. G. Singh, D .G. Desai, G. D. Patra, S. Sen and S.C. Gadkari, Phys. Stat solidi-Rapid Research Letter; 9 (2015) 530.
9. Moslem Amiri et al., J Radio. Anal. Nucl. Chem., 303 (2015) 583.
10. Siavash Yousefi, Luca Lucchese, IEEE Trans. on Nucl.Sci., 55 (2008) 2739.

Rapid Composting Technology for Decomposition of Biodegradable Wastes

Poulomi Mukherjee, Darshana Salaskar and Prasun K. Mukherjee*
Nuclear Agriculture and Biotechnology Division

Abstract

A cellulolytic fungal strain, *Trichoderma koningiopsis*, has been isolated from nature and a formulation was developed. This strain has been established as a decomposer for diverse materials like kitchen wastes and dry leaves over varied environmental conditions (seasons, locations). A user-friendly commercial technology named "Rapid composting technology for decomposition of dry leaves, kitchen waste and temple waste" has been established. Within 3 years of launching, the technology has been transferred to 22 companies, NGOs and Societies. Six products are available in the market and e-commerce portals. This technology has also been implemented at various DAE sites and institutes across the country.

Keywords: Trichoderma, Cellulase, Plant biomass, Kitchen waste, Composting, Biodegradation.

Introduction

In Nature, all that undergoes deterioration and death, on decomposition, provide raw materials for fresh growth. This is how sustainable natural systems have been maintained since aeons [1]. However, post-industrial revolution, artificial/man-made systems/materials have taken-over the reins and have started affecting the ecosystems adversely. Here, production and consumption being the major arms, wastes arising from manufacturing and use are dumped without recycling. This rapid disruption of natural cycles has led to ecosystem degradation and contributed to climate change. Rapid urbanization and population explosion have only made the problems worse. Cities are responsible for the highest net production of wastes due to high density of population and diverse economic activities. Low profitability, convenience and other economic considerations limit recycling or reuse. While the biomass is generated in rural areas, the left-overs/wastes end-up in dumping grounds in cities. In an ideal situation, the wastes should be composted and sent back to farms for enriching agricultural land where these materials were cultivated in the first place. Here, it is pertinent to mention that the "Solid Waste Management rules of 2016" (Union Ministry of Environment, Forests and Climate Change (MoEF&CC)) mandates bulk generators of waste to process their refuse at the site of generation. These rules have also emphasized on incentivising sale of compost originating from cities [2]. Effective realization of these objectives to preserve the environment and to sustain future productivity necessitates availability of a simple, rapid and feasible de-centralized composting solution. Here, we describe here one such technology that offers an easily adoptable, affordable solution to process garden waste (dry leaves, including coconut leaves), kitchen waste and floral wastes in a sustainable and eco-friendly manner.

Technology development

The basic principle behind developing this technology was to mimic natural processes of degradation and also make it eco-friendly, easy-to-adopt with low overhead costs. It is well established that natural processes of biodegradation are dominated first by a mesophillic phase characterized by degradation of long chain molecules. As bio-degradation proceeds in this phase, a rise in temperature due to the metabolic activities results in mesophiles being replaced by thermophiles. Accelerated degradation due to physical and biological activities ensues, followed by a phase of decreasing temperature which brings back the mesophiles. Several microorganisms like bacteria, fungi and actinomycetes participate in this process with succession of species from one phase to another. Microorganisms, owing to their large repertoire of enzymes (or biocatalysts)

Fig.1: *Trichoderma koningiopsis* on mango tree bark (a) and in pure culture (b)

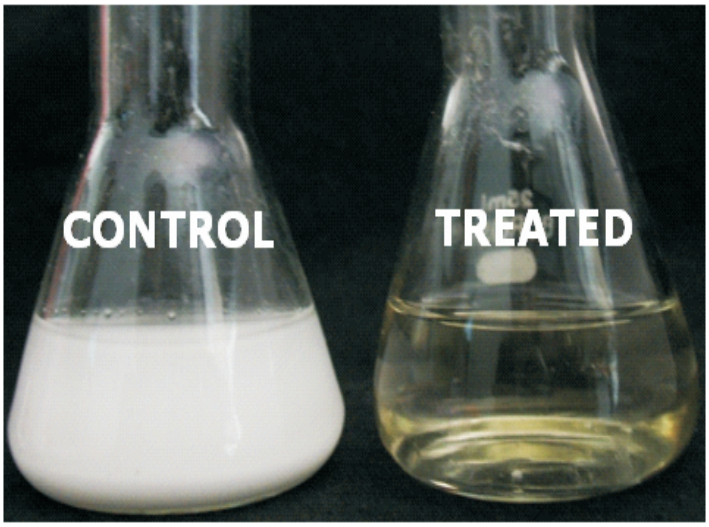

Fig.2: Cellulose utilization by *Trichoderma koningiopsis*

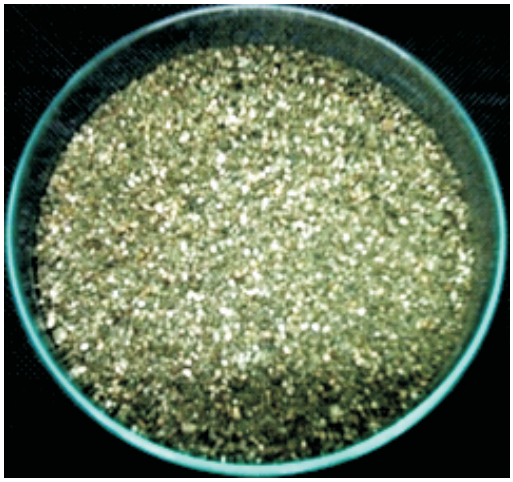

Fig.3: *Trichoderma koningiopsis* based formulation developed for biomass degradation

are versatile at degrading wastes [3,4,5,6]. Of the molecules present in biodegradable waste, the most abundant constituent is a natural polymer named cellulose. Hence it was pertinent to find a microorganism which is able to efficiently degrade this natural polymer as well as qualify as safe for humans and animals. We isolated a fungus *Trichoderma koningiopsis* from the bark of a mango tree (Figure 1 a & b); this fungus exhibited high cellulolytic activity (Figure 2). Further, a formulation (Figure 3) was developed for ease of application and storage [7].

The potential of this fungus to degrade various forms of waste particularly dried leaves, mixed food waste, floral wastes from temples, lawn mowings and tree sheddings was established in small-scale laboratory set-ups, followed by pilot studies in drums of 100 kg capacity and finally, at large scale (tonnes) at the actual waste generation/processing sites (Figure 4). Design of bins, drums and pits for containment and processing of waste materials was optimized. Discarded drums used for chemical solvents were found to be suitable after providing proper perforations for aeration (Figure 4a). This also ensured recycling of these containers and fulfilled economic considerations of a waste processing activity with apparent low pay offs.

Development of protocols for degradation of various types of biomass

The formulation was applied to compost various types of biomass at a laboratory scale of 500gms of substrate to pilot scale of 10 kgs in perforated buckets or drums. Protocols were developed for each biomass type by applying different doses of culture and adsorbent

(like coco peat), optimizing frequency of upturning and applying water wherever necessary. A general schematic representation is included (Fig. 5). Shredders of various capacities were employed and tested for different substrates like coconut leaves, common garden waste and kitchen waste. Similarly, extent of shredding was also standardized for different wastes. However, in cases where biomass or waste generated was low in amount and relatively soft in integrity (like kitchen waste or floral waste), manual chopping is recommended.

On-site implementation of the technology

The technology has been successfully demonstrated and implemented at various DAE sites and Cooperative housing societies in response to requirements from the users.

I. Kurla Kamgaar Nagar cooperative housing society

This society, situated in Mumbai, is a large housing complex with about 400 coconut trees in their premises. The BARC composting technology was transferred to this Society and successfully implemented to process "very difficult to degrade" coconut leaves within 45-55 days (Fig. 6 & 7). These leaves otherwise take more than a year to decompose under natural conditions. Implementation of this technology in their premises not only led to reclamation of dumping site within the housing society but also, the compost generated was utilized to develop as a garden manure. This technology helped the housing society to become self-sufficient in processing their own waste without sending any biodegradables outside their premises. The society bagged "The Green Society Award 2017", jointly conferred by the Maharashtra

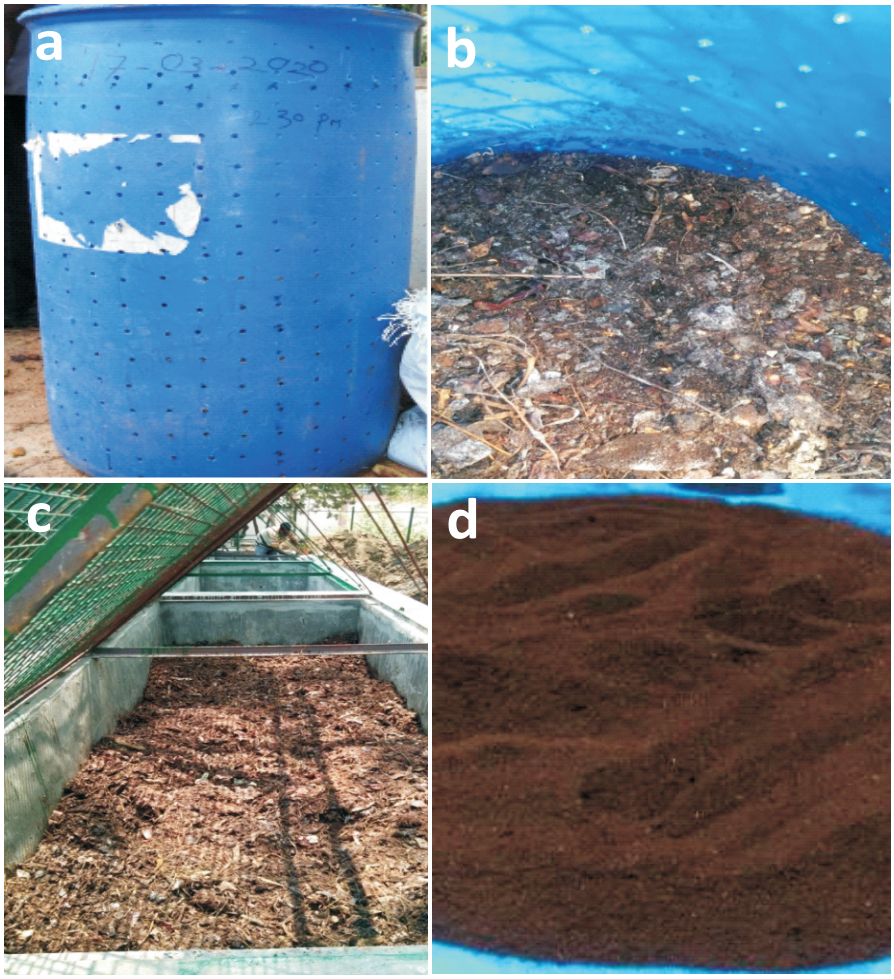

Fig.4: Composting of kitchen wastes in drums (a and b) and pit (c) and final compost derived thereof (d)

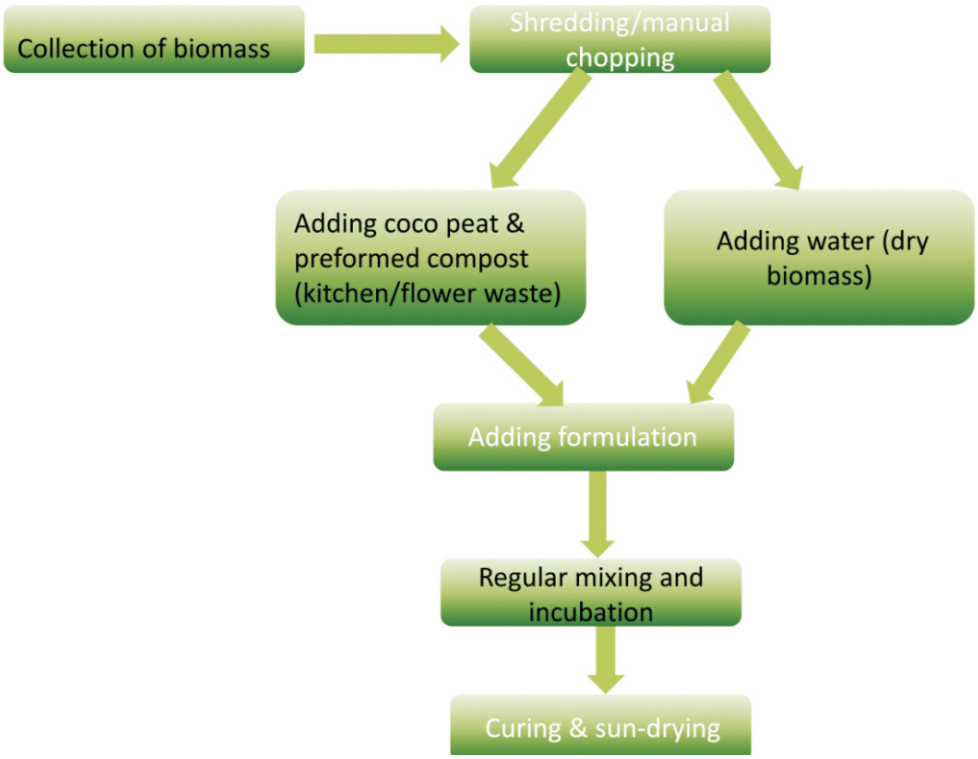

Fig.5: Schematic of the protocol for composting using formulation

Fig.6: Waste processing/composting sites. Zero waste project at Kurla Kamgar Society at Mumbai (a), Kitchen waste composting site at Mandala DAE colony (b), Canteen waste composting at Homi Bhabha Centre for Science

Fig.7: Composting of coconut leaves in pit. Initial stage after shredding (a), Composted coconut leaves after 55 days (b)

Pollution Control Board and the "Loksatta". Over a period of 4 years, more than 2.5 metric tons of coconut leaves have been converted into organic carbon-rich compost. This project is backed by Brihanmumbai Municipal Corporation and has also become a role model for other societies.

II. Anushaktinagar (DCSEM, DAE)

Floral wastes generated at religious places during festivals are a major source of pollution of water bodies during immersion. Composting of such waste (Nirmalya) offers an eco-friendly solution to this. BARC's composting technology was successfully implemented in collaboration with DCSEM, DAE at Anushaktinagar during Ganapati festival of 2019 (Figure 8). At each of the five pandal and at the immersion site, two drums containing the formulation, coco peat and preformed compost were kept. Daily offerings of flowers and leaves were added with regular mixing as per protocol. Within 15 days of the last addition of fresh flower waste, good quality compost was obtained (Figure 8).

III. Mandala Colony (DCSEM, DAE)

The kitchen waste generated at Mandala village colony near Anushaktinagar is being processed using BARC technology for more than two years (Figure 6). The colony of 100 households has been generating about 50kgs of waste per day, which is collected and chopped manually by a a

Fig.8: Nirmalya composting at Anushaktinagar DAE colony during Ganapathi festival 2019. Ganapathi pandal (a), Drums for floral waste composting (b), Shredded flowers (c), Shredded flowers after 5 days of composting (d) Shredded flowers after 10 days of composting (e) and final product (f).

a solitary contract worker. The waste is mixed with preformed compost, cocopeat and fungal formulation in appropriate proportions, and left idle in the drums for two weeks. The drums are rolled on the ground once in a day to ensure proper aeration and mixing of the contents to prevent formation of anaerobic pockets. The material obtained after 2 weeks is dried in the sun for a few days, sieved to remove un-degraded or partially degraded items like roots, stems and onion peels and left for curing (a stabilisation process accomplished by storage in shade) for another week. The un-degraded matter from the first cycle goes as feed in the next cycle of composting along with fresh waste while the cured compost is used as manure or it is bagged. This facility has been established as a model for community level composting. This site is used for training and demonstration for new technology licensees of BARC as well as individual societies and institutes. It is note-worthy that though this composting unit is situated next to residential buildings and an adjoining temple, there have been no complaints on any foul odour. Due to simplicity of the process, a single unskilled worker can manage the entire facility (with some initial training) without any need for mechanization.

IV. Other DAE sites

Organizations like Tata Institute of Fundamental Research (Figure 9), Homi Bhabha Centre for Science Education (Figure 6) and NPCIL Kakrapar (Figure 6) have successfully set up such composting facilities. This has led to a drop in environmental pollution, additional benefits, including cost-cutting, manure availability as well as employment for the economically deprived sections.

Utilization of compost

Rampant use of chemical fertilizers coupled with poor agricultural practices have made soils in India deficient in organic carbon, which is essential for sustaining crop productivity. In the present study (Table 1), the maximum total C(%) present in garden leaf compost (36.7-38) is higher than the reported values of total C (%) in FYM which is in the range of 31.9-32.9. Other composts generated have carbon content (%) varying from 21 to 29 [9]. Application of compost is the best way to replenish the soil organic matter. This also facilitates locking-up of carbon in the form of humus which in turn encourages microbial activity in the soil enhancing nutrient mobilization to crops, while minimizing green-house gas emission [8]. The nutrient value of the composts generated from multiple substrates was determined (Table 1). Plant growth experiments in pot-based studies showed significant improvement in biomass and lengths in treatments with various composts when compared with untreated control (soil without compost treatment) (Figure 10).

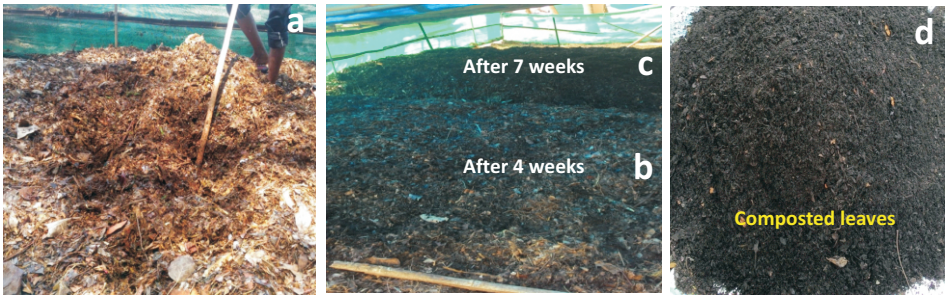

Fig.9: Composting of dry leaves from Barrintonia, Almond and Ficus trees at TIFR, Colaba. Initial stage (a), after 4 weeks (b), after 7 weeks (c) and final compost (d).

Table 1. Physicochemical parameters of different composts

Types of compost	pH	C (%)	N(%)	P(%)	K(%)
Kitchen waste compost	6.8	29.4	2.4	2.01	2.8
Coconut leaf compost	6.96	28.3-31.9	1.32-1.55	0.94	2.69
Garden leaf compost	7.14	36.7-38	2.2-2.45	0.25	1.3
Temple waste compost	7.3	21.6	0.7	0.87	1.36

Fig.10: Effect of application of different composts on growth of maize plants. Control (a), Kitchen waste compost amendment (b) Leaf compost amendment (c), Combined application of kitchen waste compost and leaf compost (d)

Technology Commercialization

The Rapid Composting technology has been very popular among the entrepreneurs. A total of 22 companies/NGOs/Housing Societies have become licensees within less than 3 years of advertising, a partial list of which is available on the website of TT&CD, BARC [10]. One of the products has become "Product of Choice" on an e-business portal and is being used extensively for household composting. We guided a start-up company in this field, which now takes-up composting projects at various places in Maharashtra, Odisha and Gujarat. This company has been successfully carrying-out a kitchen waste and garden waste composting project for a society of 600 flats at Malad, Mumbai for more than 6 months now. The technology is advertised in BARC website [11].

Conclusion

This article reflects how knowledge obtained from scientific research can be translated for solving societal and environmental problems (here, waste management).Through deployment of this technology, it's not only the ecosystem that could be saved, but also improve the working conditions for people employed in dumping grounds. This method, being completely aerobic in nature, is devoid of foul odour and hence has greater acceptability in the society. At lower scale of waste generation (till 100 kgs of waste per day), mechanization is not essential, both capital investment as well as maintenance costs are minimal. Even at higher scale (tonnes), the initial investment is very low with no need for erecting a permanent structure (except a shed and few pits). It is reiterated that economic and environmental costs of transportation and dumping of waste

far outweighs the investments for larger composting facilities. As far as manufacturing the formulation is concerned, it is easier to maintain and grow a single microbe in a commercial production facility as opposed to multiple organisms or a consortium. It is easy to multiply on cheaply available substrates and grows at ambient temperatures, allowing the cost of manufacturing to be low, thus making it an attractive option for manufacturers including Micro, Small & Medium Enterprises (MSMEs). Further the versatility in terms of different wastes that can be handled adds to the commercial viability and societal applicability. One unique advantage is that a complete segregation is not required, which makes this technology hassle-free and less labour-intensive.

This technology is an important contribution towards the Swachh Bharat Mission of the Govt. of India. Additionally, waste is being converted to wealth, by way of product arising from refuse, that goes back to nature ensuring continuation of biogeochemical cycles and replenishing soils with vital nutrients.

***Corresponding author**

Dr. Prasun K. Mukherjee

Acknowledgements

S. N. Pardeshi HBCSE, Mumbai, R. Gumaste, TIFR Colaba, Stree Mukti Sangathana, Mumbai, DCSEM, DAE, Mumbai, Shrikrishna Gupta ex Head TTCD, G.R. Ursal TTCD, Dr A. Banerji Head TTCD, BARC, Smita Mule Head AKRUTI and staff of AKRUTI, BARC, Kurla Kamgar Society, Official at NPCIL Kakrapar, R.B. Patil and Dr. A.K. Patra ESL Kakrapar, A.D. Chavan NABTD for preparation of formulation, Dr. S.P. Kale, ex-AD (BSG), Dr. S. Chattopadhyay, ex-GD (BSG), Dr. V. P. Venugopalan ex-GD (BSG), Dr. P. Suprasanna ex-Head, NABTD, Dr. S. K. Ghosh, AD (BSG).

References

1. http://en.wikisource.org/wiki/brundtland_Report/Chapter_2_towards_sustainable_development Accessed in June 2020.
2. https://www.downtoearth.org.in/news/waste/solid-waste-management-rules-2016-53443 Accessed in June 2020.
3. F. Buyuksonmez, R. Rynk, T.G. Hess, E Bechinski. Occurrence, degradation and fate of pesticides during composting. Part II: occurrence and fate of pesticides in compost and compostingsystems. Compost Science & Utilization., 8, (2000): 61–81. doi:10.1080/1065657X.2000.10701751.
4. M.S.Pedro, S.Haruta, K. Nakamura, M. Hazaka, M. Ishii, Y. Igarashi. Isolation and characterization of predominant microorganism during decomposition of waste materials in a field–scale composter. Journal of Bioscience & Bioenggineering.; 95 (2003): 368–373. doi: 10.1016/S1389-1723(03)80069-5.
5. P.D. Schlock, A.G. Hay, D.B. Wilson, LP Walker. Tracking temporal changes of bacterial community fingerprints during the initial stages of composting. FEMS Microbiology Ecology, 46, (2003): 1–9.doi: 10.1016/S0168-6496(03)00153-3.
6. G. Zing, Z. Yu, Y. Chen, J. Zhang, H. Li, M. Yu, and M. Zhao. Response of compost maturity and microbial community composition to pentachlorophenol (PCP)-contaminated soil during composting. Bioresource Technology, 102, (2011): 5905–5911.doi: 10.1016/j.biortech.2011.02.088.
7. Y. Batta, M. Rahman, K. Powis, G. Baker, O. Schmidt. Formulation and application of the entomopathogenic fungus: Zoophthoraradicans (Brefeld) Batko (Zygomycetes: Entomophthorales). Journal of Applied Microbiology, 110 (2011): 831-839. doi:10.1111/j.1365-2672.2011.04939.x.
8. Rattan Lal, Restoring soil quality to mitigate soil degradation, Sustainability, (2015): 7(5), 5875-5895; https://doi.org/10.3390/su7055875.
9. B.B. Basak, D.R. Biswas and R.K. Rattan. Comparative effectiveness of value-added manures on crop productivity, soil mineral nitrogen and soil carbon pools under maize-wheat cropping system in an Inceptisol. Journal of the Indian Society of Soil Science, 60, No. 4, (2012): 288-298.
10. https://technologies.britatom.gov.in/licensees Accessed in June 2020.
11. http://barc.gov.in/technologies/bio_composting/index.html Accessed in June 2020.

Back Page Photo: Homi Jehangir Bhabha in Trombay. Undated Photo
(DAE Archives)

Edited & Published by:
Scientific Information Resource Division
Bhabha Atomic Research Centre, Trombay, Mumbai 400 085, India
BARC Newsletter is also available at URL:http://www.barc.gov.in